npj | Flexible Electronics

www.nature.com/npjflexelectron

ARTICLE OPEN

Check for updates

Single and bundled carbon nanofibers as ultralightweight and flexible piezoresistive sensors

Debarun Sengupta[1,2], Ssu-Han Chen[2], Aron Michael[2], Chee Yee Kwok[2], Sean Lim[3], Yutao Pei[1] and Ajay Giri Prakash Kottapalli[1,4]✉

This work demonstrates the application of electrospun single and bundled carbon nanofibers (CNFs) as piezoresistive sensing elements in flexible and ultralightweight sensors. Material, electrical, and nanomechanical characterizations were conducted on the CNFs to understand the effect of the critical synthesis parameter—the pyrolyzation temperature on the morphological, structural, and electrical properties. The mechanism of conductive path change under the influence of external stress was hypothesized to explain the piezoresistive behavior observed in the CNF bundles. Quasi-static tensile strain characterization of the CNF bundle-based flexible strain sensor showed a linear response with an average gauge factor of 11.14 (for tensile strains up to 50%). Furthermore, conductive graphitic domain discontinuity model was invoked to explain the piezoresistivity originating in a single isolated electrospun CNF. Finally, a single piezoresistive CNF was utilized as a sensing element in an NEMS flow sensor to demonstrate air flow sensing in the range of 5–35 m/s.

npj Flexible Electronics (2020)4:9 ; https://doi.org/10.1038/s41528-020-0072-2

INTRODUCTION

Technological advancements made over the past few decades in soft material processing and nanofabrication techniques have led to substantial progress in the development of flexible and wearable sensors. The demand for ultrathin, portable, and wearable sensors is the main fueling factor behind the rapid advancement in soft and flexible material processing technologies. Traditional piezoelectric materials like lead zirconate titanate (PZT), barium titanate, and zinc oxide have mainly been explored for developing sensors and energy harvesters in the past[1–6]. Though PZT was immensely successful primarily because of its high piezoelectric coefficient, alternative materials (both organic and inorganic) have been explored and investigated by researchers due to the presence of lead in the material composition. In addition, the brittle nature of PZT ceramics disqualifies its usage in wearable applications where large pliability is required. Soft piezoelectric polymer materials like polyvinylidene fluoride (PVDF) and its copolymers like polyvinylidene fluoride-trifluoroethylene (PVDF-TrFE) were identified as alternatives to PZT because of their low cost, mechanical flexibility, and biocompatibility. In particular, PVDF-based flexible energy harvesters and self-powered sensors have been extensively studied[7–11]. In addition to thin film-based devices, electrospun nanofiber-based flexible and wearable devices and energy harvesters leveraging on the piezoelectric property of materials like PVDF have been extensively researched[7,12–16]. Electrospinning is an inexpensive and time-efficient method to fabricate large area of nanofiber mats/membranes. In addition, electrospinning has also been proven to be a simple and effective method for fabricating fairly complex sensors, which would otherwise have been difficult to produce with traditional microelectromechanical systems (MEMS) fabrication techniques[13,17].

The fundamental problem with using piezoelectric nanofibers for strain sensing applications lies in the fact that piezoelectric materials like PVDF respond only to dynamic stimulus. For static strain sensing applications, traditional strain gauges are still the preferable choice. In contrast, the concept of flexible sensors utilizing the piezoresistive property of flexible polymer materials is relatively new, and researchers across the world are investigating novel nanomaterial−polymer composites for developing wearable and flexible sensors[18–23]. Various conductive carbon-based nanomaterials, like graphene, carbon nanotubes (CNTs), carbon nanofibers (CNFs), and carbon blacks (CBs) have been explored by researchers[19,21,23–31]. Also, various elastomeric materials like ecoflex, polyimide (PI), rubber, polydimethylsiloxane (PDMS), and polyurethane (PU) have been commonly used as the flexible polymer substrates due to their superior mechanical properties including compressibility, stretchability and excellent responsiveness to tension and torsion[19,21,22,32,33]. However, for most of the works reported in the literature, either fragile free-standing foamy graphene structures were employed or the fabrication process involved sophisticated multistep process comprising of polymer infiltration in a graphene-coated template and subsequent etching. The concept of using electrospun CNF bundles as the principle sensing element is comparatively new and needs further exploration as it can prove to be a cheaper and easier to acquire alternative to the more expensive nanomaterials like graphene and CNTs. In one of the pioneering works, Zussman et al.[34] characterized the mechanical and structural properties of graphitized electrospun polyacrylonitrile (PAN) nanofiber-based CNFs. In another work, Cai et al.[35] reported the piezoresistive property of individual electrospun CNF. However, beyond the fundamental characterization of electrospun PAN nanofiber-based CNF, their utilization in developing flexible sensors has not been explored. Moreover, the onset of piezoresistivity in electrospun CNF and the

[1]Department of Advanced Production Engineering (APE), Engineering and Technology Institute Groningen (ENTEG), University of Groningen, 9747 AG Groningen, The Netherlands. [2]School of Electrical Engineering & Telecommunications, The University of New South Wales, Sydney, NSW 2052, Australia. [3]Mark Wainwright Analytical Center, The University of New South Wales, Sydney, NSW 2052, Australia. [4]MIT Sea Grant College Program, Massachusetts Institute of Technology (MIT), 77 Massachusetts Avenue, NW98-151, Cambridge, MA 02139, USA. ✉email: a.g.p.kottapalli@rug.nl

Published in partnership with Nanjing Tech University

npj nature partner journals

change in morphological properties due to the pyrolyzation temperature are not well understood. Given the flexibility, lightweight and possibly high piezoresistive coefficient of PAN-based CNFs, there is immense scope for further research in developing flexible sensors and their utilization as sensing elements in nanoelectromechanical systems (NEMS) sensors. Single isolated electrospun CNFs have been reported to have gauge factors in the range 1.96−2.55 [35]. However, further investigation is required to understand the effect of critical processing parameters such as the pyrolyzation temperature on the conductivity of the nanofibers and their piezoresistive behavior. In addition to the modest piezoresistive gauge factor of a single CNF, a bundle of nonwoven CNFs can achieve a high piezoresistive gauge factor by the virtue of their conductance path change under the influence of strain arising from external stress.

In this work, extensive experimental studies were conducted to understand the effect of different pyrolyzation temperatures on the microstructure, morphology, and electrical properties of electrospun PAN-based CNFs. Various spectroscopic and microscopic characterization experiments including Raman, X-ray photoelectron spectroscopy (XPS), FESEM and TEM analyses were conducted to explain the early onset of piezoresistivity in relatively low temperature (compared to other works in literature) pyrolyzed electrospun PAN nanofiber bundles. The onset of piezoresistivity at relatively low temperatures as compared to previous works was hypothesized by invoking graphitic domain discontinuity model. Electrospun PAN nanofibers pyrolyzed at temperatures as low as 950 °C were used as piezoresistive sensing elements to demonstrate two distinct modes of operation involving single CNF and bundled CNFs. Ultralightweight and flexible strain sensors were demonstrated that use the conductive property of the electrospun CNF bundle combined with the effect of the change of its conductance path when subjected to external stress. Quasi-static tensile strain characterization experiments conducted on the CNF bundles embedded in PDMS demonstrated a linear response with an average gauge factor of 11.14 for tensile strains up to 50%. The response of the flexible strain sensors was tested for both static and dynamic strain stimuli. In addition, this work for the first time successfully demonstrates the feasibility of applying the piezoresistive property of a single isolated CNF for sensing applications and electrospun PAN-based CNF bundles for wearable and flexible sensor applications. The piezoresistive effect of a single CNF was demonstrated via air flow sensing with a fabricated NEMS sensor which featured an isolated single CNF as the sensing element. The single CNF flow sensor was tested for air flow sensing with a wind flow velocity in the range 5–35 m/s. The proposed method of using electrospun CNF bundles as strain and flow sensors could potentially alleviate the complex microfabrication methods for developing piezoresistive strain gauges.

RESULTS

Study of pyrolyzation and piezoresistive nature of PAN nanofibers

Morphology characterization of the pyrolyzed nanofiber mats. Microscopic inspection of the nanofibers provides qualitative information regarding the shrinkage of nanofiber diameters induced by the carbonization process. The electrospun PAN nanofiber bundles were subjected to five different pyrolyzation temperatures at 500, 600, 700, 800, and 950 °C for 1 h. The diameters of pyrolyzed nanofibers were measured and recorded as shown in Fig. 1a–f. Six diameter measurements were taken for each bundle annealed at the aforementioned temperatures and the average diameter is presented in Fig. 1g. Overall, the diameters of the nanofibers were observed to have shrunk by a percentage of 20, 40, 50, 55 and 60% for pyrolyzation temperatures of 500, 600, 700, 800, and 950 °C respectively. Pyrolyzation-induced diameter reduction is in agreement with the past works carried out by Zussman et al.[34] and Kim et al.[36]. The phenomenon can be explained by assuming that the nanofibers undergo weight loss due to the breaking of carbon−oxygen and carbon−nitrogen bonds and subsequently releasing oxygen and nitrogen and densification due to the formation of carbon−carbon bonds. Also, a comparative analysis of the SEM images of the as-spun nanofibers with the carbonized nanofibers reveals a smoothening effect on the outer surface of the nanofibers induced through the pyrolyzation process (Supplementary Fig. 2).

Understanding graphitic ordering employing Raman spectroscopy. Figure 2 shows the Raman spectra of the nanofiber bundles annealed at the aforementioned pyrolyzation temperatures. Mixed Gaussian−Lorentzian functions were fitted and the integrated intensities of the individual D- and G-peaks (I_D and I_G respectively) were calculated. In past, Knight and White proposed an empirical formula for the calculation of crystallite size (L_a) of the individual graphitic crystals inside graphitic carbons and other sp^2-bonded carbons from the "*R*"-value (the ratio of integrated peak intensities, I_D/I_G)[37], which is valid for wavelengths near $\lambda_l = 514.5$ nm [38]. The more general expression for L_a is given by[38]:

$$L_a(\mathrm{nm}) = C(\lambda_l)\left(\frac{I_D}{I_G}\right)^{-1}, \quad (1)$$

where $C(\lambda_l)$ is a variable scaling coefficient and can be determined using the formula: $C(\lambda_l) \approx C_0 + \lambda_l C_1$ for a particular wavelength ($400 < \lambda_l < 700$ nm). More details regarding the variable scaling coefficient are provided in the supplementary information section (Supplementary Fig. 3).

The *R* values and the size of nanographitic crystallites were calculated for all the nanofiber bundles pyrolyzed at different temperatures and are listed in Table 1. From Table 1, it can be observed that there is a steady increase of L_a with increasing pyrolyzation temperature. Raman analysis presented here provides evidence that carbonization can take place below 700 °C, though the graphitic nano-crystallites would be smaller in size and will have a higher content of defects as compared to the nanofibers pyrolyzed at higher temperature.

Understanding the compositional change and hybridization states of carbon by employing XPS analysis. To study the change in surface/overall composition of the nanofibers with varying pyrolyzation temperature, XPS spectra were recorded for the as-spun nanofiber bundle, stabilized nanofiber bundle and nanofiber bundle pyrolyzed at 950 °C. As seen in Fig. 3a, an overall increase in the carbon content (relative percentage) and a decrease in nitrogen content were observed after the pyrolyzation step. The changes in the composition of the nanofiber bundles are tabulated in Fig. 3a inset. As-spun PAN nanofibers ideally do not contain oxygen. Stabilization of the as-spun nanofibers in the presence of air causes the incorporation of oxygen in the nanofiber bundle by the formation of carbon−oxygen single (C−O−C) and double (C=O) bonds. Therefore, a sharp increase in the oxygen content in the nanofiber bundle and a relative drop in carbon content was observed. When the stabilized bundles were annealed in an N_2 ambient, decomposition of carbon−nitrogen double bonds (C=N), carbon−oxygen single (C−O−C), and double (C=O) bonds occur. After reaching the carbonization temperature of 700 °C, there is a sharp decrease in nitrogen content with increasing annealing temperature, which can be attributed to the breaking of carbon−nitrogen double (C=N) bonds and releasing of nitrogen. Overall, with increasing pyrolyzation temperature, an increase of relative carbon content is observed that explains the dominance of G peak as seen from the Raman spectra. As the carbon−oxygen single/double bonds and carbon−nitrogen bonds break, carbon−carbon bonds are formed that leads to a densification of the bundles and hence

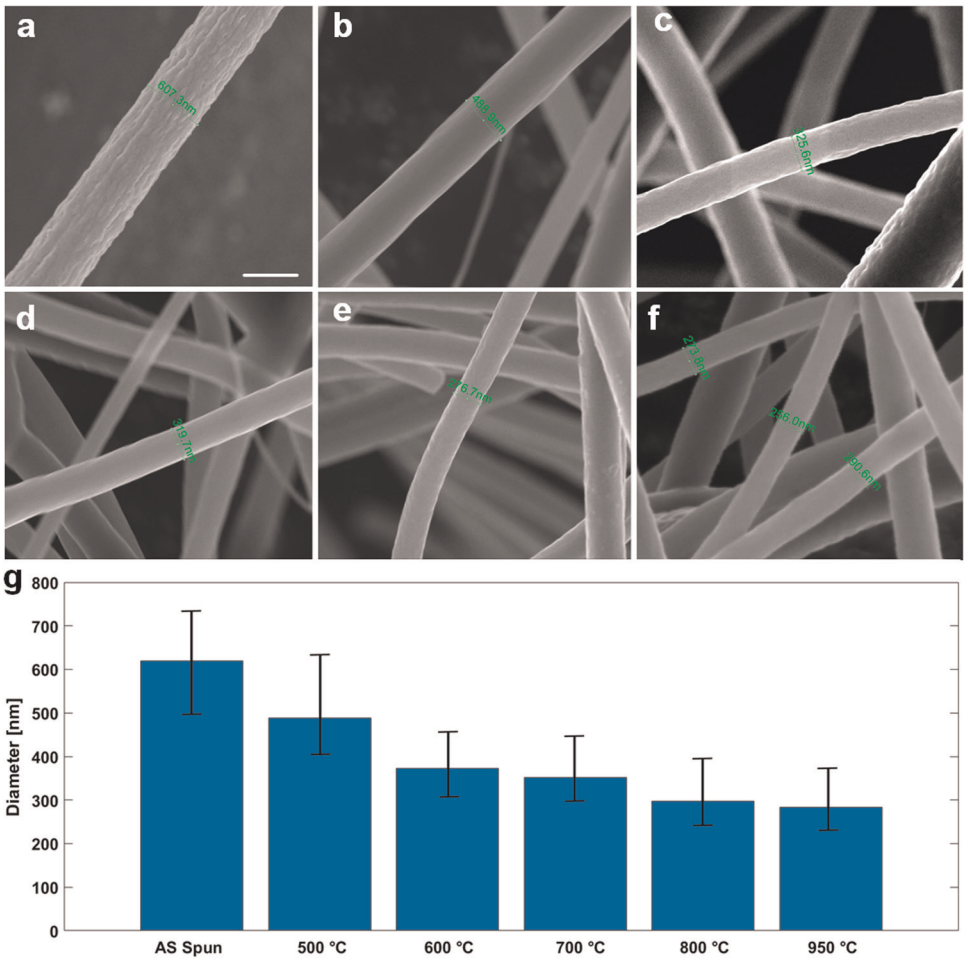

Fig. 1 FESEM images showing the diameter evolution of individual nanofibers of **a** as-spun PAN nanofiber bundle and nanofiber bundle pyrolyzed at **b** 500 °C, **c** 600 °C, **d** 700 °C, **e** 800 °C, **f** 950 °C. **g** Bar graph demonstrating the overall decrease in nanofiber diameter with error bars depicting standard deviation. Scale bars (**a**–**f**) = 500 nm.

shrinkage in the overall diameters of the nanofibers as observed from FE-SEM micrographs.

The acquired C1s spectrum for the nanofiber bundle annealed at 950 °C was analyzed to determine the fraction of sp^2- and sp^3-bonded carbon atoms as shown in Fig. 3b. The C1s spectrum was deconvoluted into three contributions using a mixed Gaussian Lorentzian fitting. From the XPS spectrum, clearly resolved peaks centered around 284.8 eV (sp^2-bonded carbon), 285.6 eV (sp^3-bonded carbon), and 289 eV (C=O bond) were identified. The fraction of sp^2- and sp^3-bonded carbon atoms was determined according to the area under the sp^2 and sp^3 peaks. The fraction of sp^2 bonds (area under the sp^2 peak divided by the sum of areas under sp^2 and sp^3 peaks) was calculated to be 0.93. The presence of sp^3-bonded carbons is supported by the D peak in Raman analysis for the nanofiber bundle annealed at 950 °C, which explains the structural disorder in the nanofiber bundles pyrolyzed at a relatively low temperature.

Observing graphitic domain employing TEM imaging. TEM micrographs of the nanofiber bundles annealed at 600 and 950 °C were obtained in order to observe graphitic crystallization and any lattice orientation within the nanofibers. For observing the fractured edge of a single nanofiber, sonicated samples as shown in Fig. 4a, b were used. From the TEM micrograph of the broken edge of the nanofiber in Fig. 4a, b, several sheath layers can be seen. Furthermore, focused ion beam milled samples were used for observing the cross-section of the nanofiber pyrolyzed at 600 and 950 °C. For the nanofiber pyrolyzed at 600 °C, no graphitic crystal domains were observed from the TEM micrograph shown in Fig. 4c. However, the cross-section micrograph of the nanofiber pyrolyzed at 950 °C reveals the presence of layered planes in parallel orientation with the skin of the nanofiber as shown in Fig. 4d. Some other crystallites were found to be misoriented with respect to the nanofiber axis.

The TEM micrographs indicate a core-shell structure for both the nanofibers pyrolyzed at the aforementioned temperatures. In addition, HR-TEM micrographs strongly indicate the turbostratic structure of the nanofibers pyrolyzed at 950 °C which were characterized by high stacking disorder[34]. In particular, the presence of strong D peak in the Raman analysis indicates the turbostratic structure of nanofibers pyrolyzed at 950 °C. Previously, Cai et al.[35] reported not to have observed any crystalline domain formation. Though the Raman analysis for the PAN nanofiber bundle annealed at 600 °C demonstrated a weak G peak signifying the formation of small graphitic domains, the TEM micrograph (Fig. 4c) of the cross-section of the nanofiber did not show any lattice domain formation, which can be attributed to a number of factors including TEM sample preparation, and the size of the individual graphitic crystallites.

Electrical characterization. To understand the effect of pyrolization temperature on the conductivity of the nanofiber bundles, 1 cm × 1 cm nanofiber mats were cut and sized. Cascade probe station was used to measure the sheet resistance of the individual

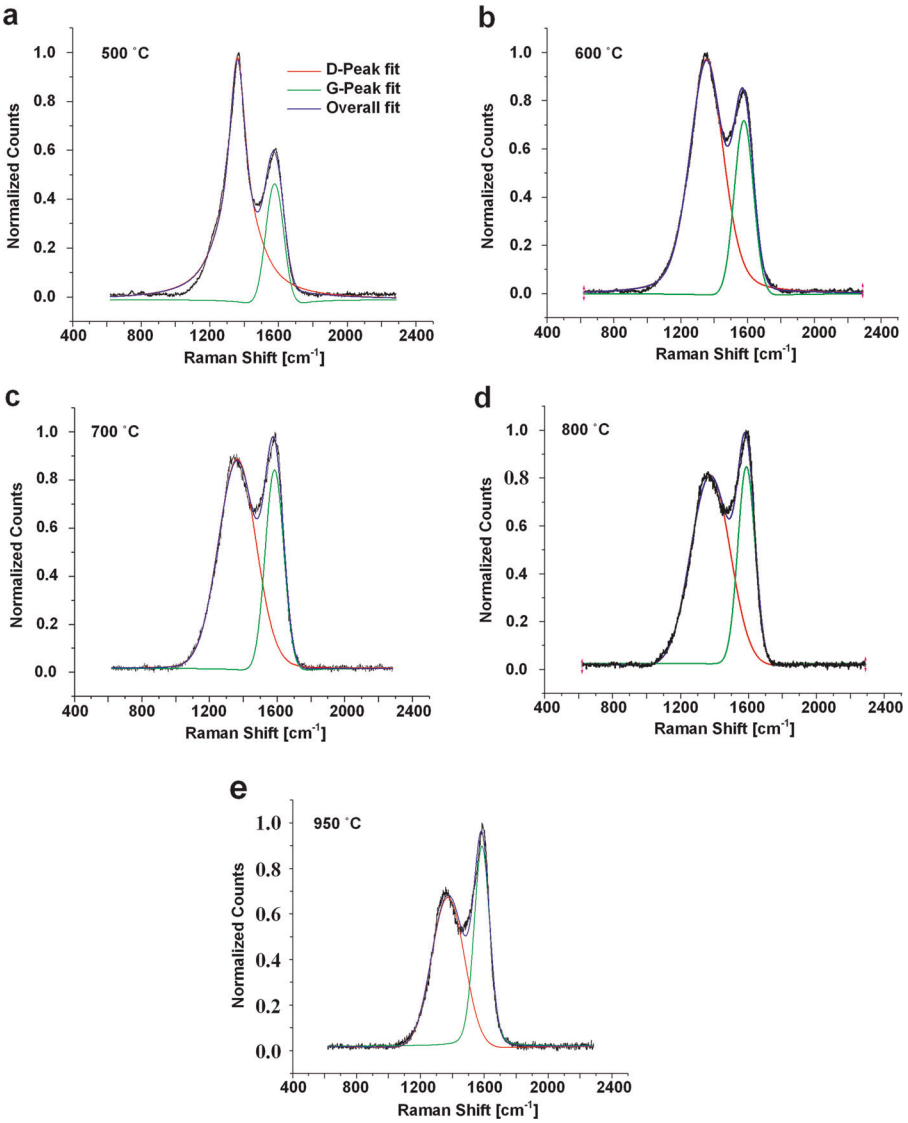

Fig. 2 Raman spectra of nanofiber bundles pyrolyzed at **a** 500 °C, **b** 600 °C, **c** 700 °C, **d** 800 °C, and **e** 950 °C.

Table 1. Tabulating the "*R*" over the range of different pyrolyzation temperatures used.

Pyrolyzation temperature (°C)	$R = \frac{I_D}{I_G}$	L_a (nm)
500	4.76	1.04
600	2.90	1.71
700	2.36	2.10
800	2.07	2.39
950	1.33	3.73

nanofibers to understand overall resistance change in the nanofiber mats with increasing pyrolization temperature. Figure 5 shows the plot of CNF bundle sheet resistances versus the corresponding pyrolization temperatures. The sheet resistance was observed to decrease sharply with an increase in pyrolization temperature from 600 to 700 °C. This was also reflected in Raman analysis where the G-peak intensity starts dominating the D-peak intensity as the pyrolization temperature changes from 600 to 700 °C. Also, the resistance of the nanofiber bundles annealed at 500 °C was found too high to be measured accurately. Again, this particular observation is in agreement with Raman analysis where the "*R*"-value decreases sharply as the pyrolization temperature was changed from 500 to 600 °C. Starting at 600 °C, the pyrolized nanofiber bundles start showing conductivity. An exponential decrease in the resistance of the CNF bundles with increasing pyrolyzation temperature was observed.

The Raman analysis clearly shows the improvement of graphitic ordering in the CNF bundles with increasing pyrolyzation temperature. The XPS analysis conducted for the CNF bundles pyrolyzed at 950 °C shows an sp^2 fraction of 0.93 signifying the dominating presence of discontinuous graphitic domains inside amorphous sp^3-hybridized carbon. TEM imaging conducted on the CNF sample at 950 °C also presents clear evidence of graphitic nano-crystallites in a matrix of nonconductive amorphous carbon. Finally, the electrical characterization points towards the enhancement of conductivity in the CNF bundle with increasing pyrolyzation temperature which supports the material characterization results. In the past, Cai et al.[35] have hypothesized that the electrical conduction in CNFs is due to the electric conduction within the graphitic domains along with the inter-domain electron tunneling. In CNFs, the conductive sp^2 hybridized regions (turbostratic domains) are embedded in a nonconductive sp^3 hybridized amorphous carbon atom matrix. The electron

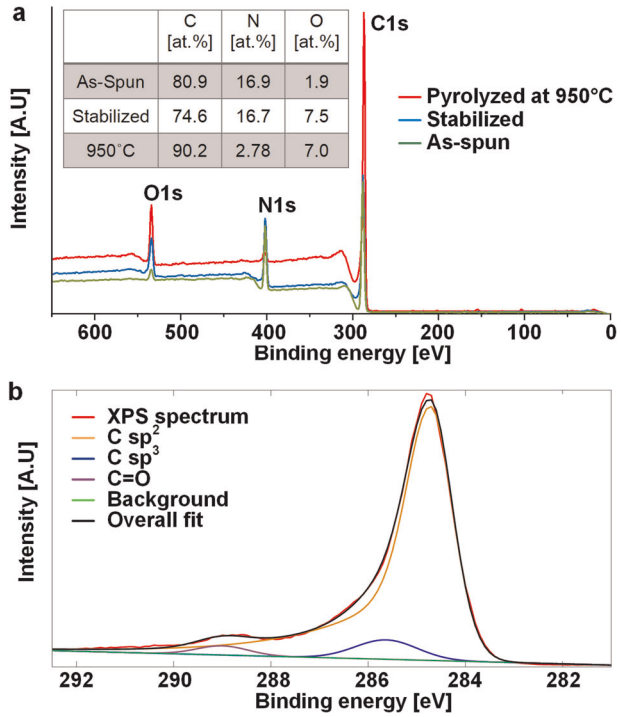

Fig. 3 XPS analysis. a Spectra of as-spun nanofibers, stabilized nanofiber bundles and nanofiber bundles pyrolyzed at 950 °C. **b** Deconvoluted C1s spectrum of nanofiber bundles pyrolyzed at 950 °C.

tunneling resistance is quite sensitive to the electron tunneling distance, leading to its high sensitivity towards local strain which explains the enhanced piezoresistive performance in CNFs in comparison to carbon fibers (microfibers) having a continuous turbostratic domain. As the electrical conductivity in the nonconductive sp^3 hybridized amorphous carbon region is mainly due to the tunneling effect, any strain resulting from applied mechanical load leads to a change in resistance owing to the change in tunneling distance. From the conductive domain discontinuity model, it can be argued that in our case, the CNFs pyrolyzed at 700 °C should show piezoresistivity owing to graphitization which is evident from the Raman spectroscopy results. Raman spectrum of the nanofibers pyrolyzed at 700 °C shows prominent dominating "G"-peak, thus indicating the formation of graphitic/turbostratic domains (Fig. 2c). Also, the electrical resistance measurement conducted on a 1 cm × 1 cm CNF bundle pyrolyzed at 700 °C shows a finite measurable resistance of 88.5 kΩ (Fig. 5), signifying the presence conductive graphitic domains inside.

Single and bundled CNFs in sensor applications

Fabrication of a bundled CNF strain sensor. Electrospinning technique was used to form both bundled PAN nanofiber films on an aluminum foil substrate and for the placement of a single nanofiber on a specially designed MEMS substrate as shown in Fig. 6a. The as-spun nanofiber film was lifted off the aluminum substrate on which they were initially spun and subjected to stabilization and subsequent carbonization at 950 °C in N_2 ambient. The photographs in Fig. 6b, c show the flexibility of the stabilized and carbonized nanofiber bundle withstanding

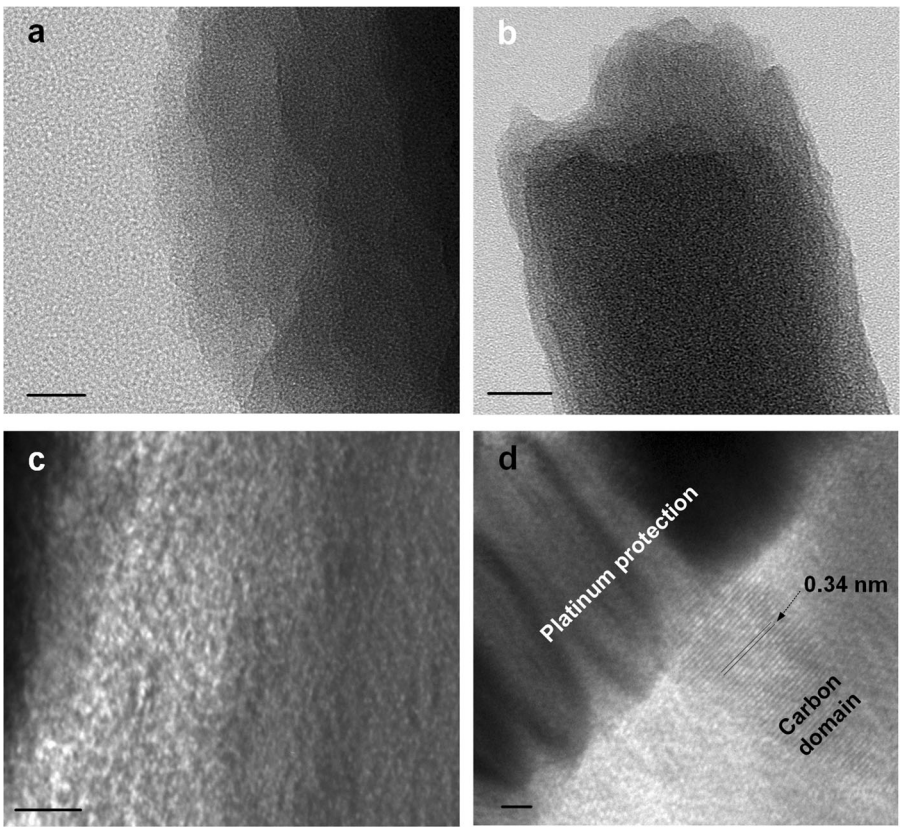

Fig. 4 TEM micrographs of the PAN nanofibers pyrolyzed at 600 and 950 °C. a, **b** TEM images of the broken edges of the nanofibers pyrolyzed at 600 and 950 °C respectively, showing the presence of several sheath layers. **c** Cross-section high-resolution TEM micrograph of the nanofiber pyrolyzed at 600 °C does not reveal any graphitic crystal domain formation. **d** Cross-section TEM micrograph of the nanofiber pyrolyzed at 950 °C showing the presence of lattice structures. Scale bars (**a**, **b**) = 20 nm; (**c**) = 5 nm; (**d**) = 2 nm.

large bending without fracturing, thus demonstrating the suitability of CNF bundles for wearable and flexible sensing applications. To suit the specific flexibility and stretchability requirements of the targeted applications, two different types of sensors were fabricated for experiments involving tensile strain sensing (CNF bundle with PDMS substrate) and static/oscillatory bending sensing (CNF bundle with optically clear adhesive (OCA) substrate). Figure 6d presents a schematic illustration of the process steps involved in the fabrication of the flexible CNF strain sensor with OCA as the substrate. A CNF bundle, 180 mm in length and 5 mm in width, was cut and transferred on to an OCA film. Seven copper tape strips were placed 25 mm apart on the base OCA film layer. The nanofiber bundle was secured by silver conductive epoxy on to the copper tape strips to improve the conductivity between the nanofibers and the copper tapes. The nanofiber bundle was sandwiched using another OCA film on top to create a strip of flexible strain sensor. OCA films have the unique property of pressure-sensitive adhesive where two films are sealed to each other when placed together in contact, thus allowing for tight sealing of the CNF bundle in between them. Dicing lines were marked and six sensors were diced out from the prepared strip. The fabricated CNF strain sensor is shown in

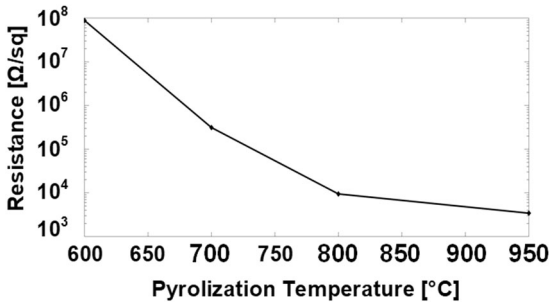

Fig. 5 Plot showing the variation of sheet resistance of the nanofiber bundles with increasing pyrolyzation temperature.

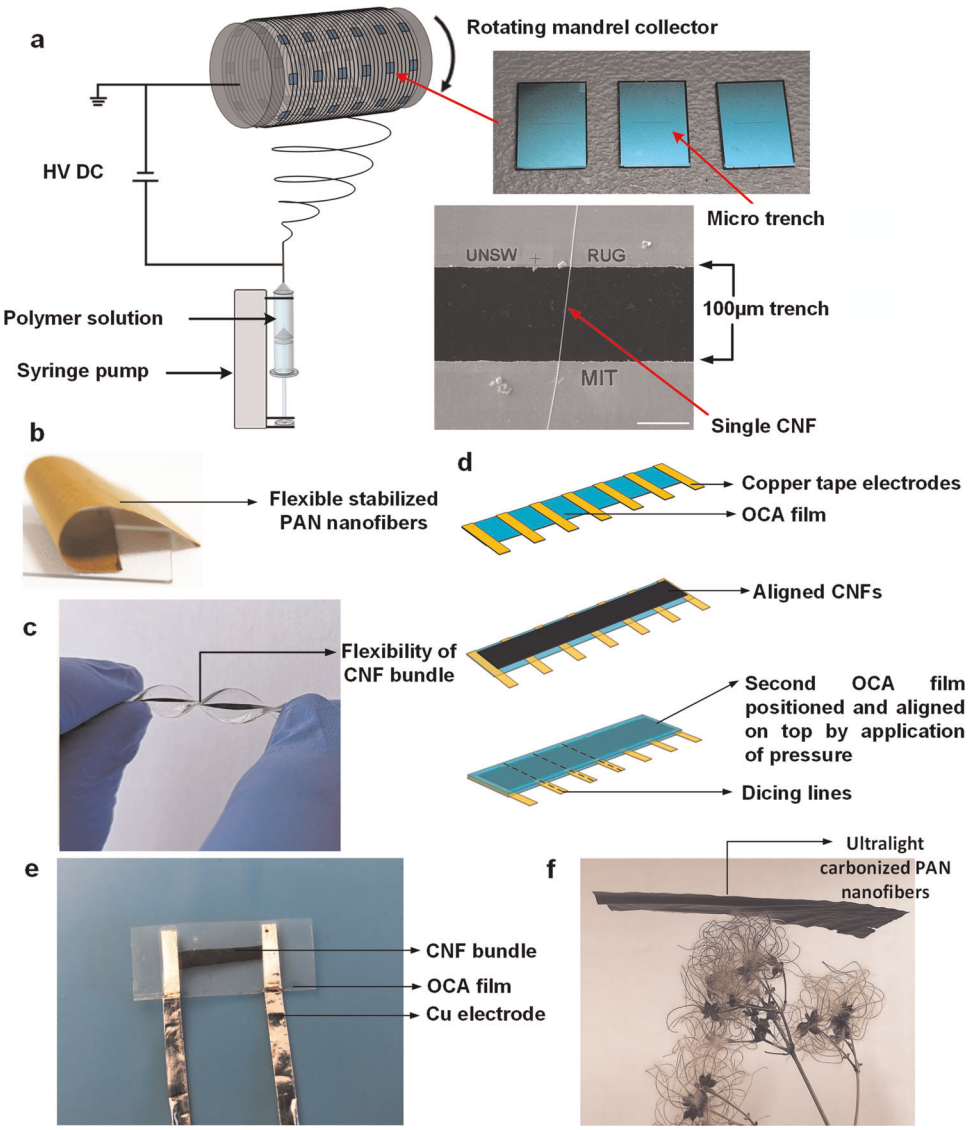

Fig. 6 CNF bundle strain sensor. a Schematic of the electrospinning setup for single PAN nanofibers across micro-trench and nanofiber bundles on an aluminum foil substrate; photograph of the fabricated micro-trench sample; SEM image of electrospun single PAN nanofibers across the micro-trench. **b** Flexible stabilized electrospun PAN nanofibers. **c** CNF bundle embedded in PDMS substrate in flexed position demonstrating excellent flexibility. **d** Schematic diagram of elements of the strain sensor. **e** CNF strain sensor in straightened position. **f** Flexible ultralightweight carbonized electrospun PAN nanofibers on a leaf. Scale bar (**a**) = 50 μm.

Fig. 6e. Since OCA as a substrate does not offer the desired stretchability required for fabricating highly stretchable elastic sensors, a rectangular thin film of bundled CNFs of dimensions of 45 × 2 mm was embedded in PDMS (thus achieving a complete encapsulation) to develop a strain sensor appropriate for tensile strain sensing applications and subsequent gauge factor characterization (Fig. 6c). The carbonized nanofibers are extremely light in weight as demonstrated in the photograph shown in Fig. 6f. A 1 cm^2 sheet of CNF bundle was found to have a mass of 310 µg, which is roughly 30 times lighter than a standard writing paper of the same dimension (9.56 mg/cm^2).

Fabrication of isolated single CNF sensor. Micro-trenches with a width of 100 µm were patterned with a photoresist mask on a silicon wafer and etched through with deep reactive ion etching to create approximately 100-µm-deep trenches. The etched samples with the micro-trenches were conformally covered with a 1-µm-thick oxide layer grown by a wet oxidation process to act as an electrically insulating barrier. An array of samples was placed on the spindle of the electrospinner with the micro-trenches aligned in perpendicular to the spindle rotating direction, as shown in Fig. 6a. An optimized time-controlled recipe was used for spinning a single PAN nanofiber on the MEMS substrate. The as-spun single nanofiber across the trench was subjected to stabilization and subsequent pyrolyzation at 950 °C in N_2 ambient to achieve an isolated single CNF. The two ends of the nanofiber were secured using conductive silver epoxy and the nanofibers were connected to a PCB by gold bonding wires. The details of the fabrication process steps and illustrations are provided in the supplementary material (Supplementary Fig. 4).

Experimental strain characterization. Quasi-static tensile strain characterization was conducted on the CNF-PDMS stretchable sensor employing a tensile stage acquired from Kammrath−Weiss to determine the gauge factor of the CNF bundle (embedded in PDMS substrate). Figure 7a schematically represents the experimental setup. The tensile loading experiment was repeated thrice, and the sensor output was logged continuously for each run of the three repetitions. The plot in Fig. 7b shows the averaged resistance change (of the sensor) in response to tensile strain over a range of 0–50%. The sensor demonstrated a linear response within the applied strain range of 50% with an average gauge factor of 11.14. Table 2 compares the gauge factor of the proposed bundled CNF-PDMS flexible sensor with other nanomaterial-based piezoresistive sensors reported in the literature.

To further demonstrate the strain sensing capability of a CNF bundle, a series of static bending, prolonged loading, and dynamic loading tests have been conducted on the CNF-OCA sensor to qualify its applicability as a wearable or pliable sensor. For the static bending test, the CNF-OCA sensor was subjected to a series of bias currents (0.5, 1.0 and 1.5 mA) and the voltage across the bundle was recorded using a digital multimeter (HP 34401a) upon bending the sensor to various radius of curvatures (ROC). At each bias current, the CNF bundle strain sensor was bent with an ROC of 8, 10, 12, 15, 18, and 20 cm, respectively. To maintain consistency between the tests, 3D printed arc brackets that correspond to the given curvatures were made. The experiments were performed by placing the strain sensor on these brackets to observe the changes in voltage with induced bending. The unstrained sensor at a flat position driven by a current of 0.5, 1.0 and 1.5 mA showed a measured voltage drop of 0.948, 1.894 and 2.83 V, respectively. The sensor demonstrated a reduction in the voltage drop upon bending which was due to the increase in the nanofiber conductive path, leading to a reduction in the resistance of the CNF bundle. The response of the sensor was found to have a highly linear relationship with bending for three different levels of bias currents as seen in Fig. 7c.

For demonstrating the capability of the CNF-OCA sensor in detecting constant pressure stimulus, a fixed mass was placed on the sensor for a time duration of 20 s. The change in the output of the Wheatstone bridge circuit to which the sensor was connected was continuously logged to observe the changes in the output voltage before, during, and after removal of the mass. Figure 7d shows the sensor response, which demonstrates that the sensor holds a very stable output through the duration of the long press of 20 s, and upon removal of the mass, it is found to return to its initial position.

To demonstrate dynamic strain sensing response of the CNF-OCA sensor, a series of cyclic strain stimuli at two different frequencies (7 and 35 Hz) were applied on the sensor. The sensor response replicated the input stimuli without any noticeable delay as seen in Fig. 7e, f.

NEMS single CNF flow sensor testing. The pyrolyzed single CNF sample bonded on to a printed circuit board as shown in Fig. 8a was secured on Hysitron PI-85 picoindenter placed inside an FE-SEM chamber to demonstrate the flexibility and stretchability of an isolated CNF. SEM micrographs in Fig. 8b, c show the positioning and stretching of the isolated CNF with the nanoindenter tip thus confirming the stretchability of an isolated CNF. The single CNF NEMS sensor was placed inside a subsonic wind tunnel to demonstrate the possibility of using the single CNF for applications such as air flow sensing. Figure 8d schematically represents the voltage divider circuit used for acquiring the sensor output when subjected to different wind flow velocities. The average output voltage change recorded by the DAQ at each velocity is plotted in Fig. 8e. The response shows an increase in voltage change with increasing velocity, which corresponds to a change in resistance of the suspended CNF with strain. The results from the wind tunnel test are in-line with the conductive domain discontinuity model explaining the piezoresistivity in CNFs.

DISCUSSION

This work fundamentally investigated the piezoresistive behavior demonstrated by CNFs and harnessing them for various sensing applications including flow velocity, strain, and static pressure that piezoelectric sensors are not able to sense. The effect of pyrolyzation temperature, which is a critical parameter for synthesizing CNFs from polyacrylonitrile precursor, was studied by employing Raman, XPS, FESEM and TEM characterization techniques. Direct electrical characterization has been conducted on the CNF bundles to understand their piezoresistive sensing capability. Also, electrical characterization has been conducted on individual electrospun CNFs in the form of wind flow stimulus vs. resistance change to understand their piezoresistive sensing capability. Possible manifestation of piezoresistivity in CNF bundles pyrolyzed at lower temperatures has also been hypothesized. Finally, the application of single and bundled CNFs in forming flexible, ultralightweight sensors was demonstrated by fabricating strain sensors, and their sensing performance was experimentally investigated through a series of static and dynamic tests. Tensile strain characterization experiments conducted on the CNF-PDMS flexible sensor demonstrated a linear response over an applied strain range of 0–50% with a gauge factor of 11.14. Various experiments involving static and dynamic loading have been demonstrated which fundamentally establish the utility of CNFs as a sensing element in flexible sensor applications. In addition, flow sensing performance assessments conducted on a single CNF-based NEMS flow sensor demonstrated the capability of the sensor in detecting static wind flow velocity in the range 5–35 m/s. This work established a facile method of developing highly sensitive, flexible, and ultralightweight piezoresistive sensors utilizing CNFs as the principal sensing elements for wearable electronics and sensors.

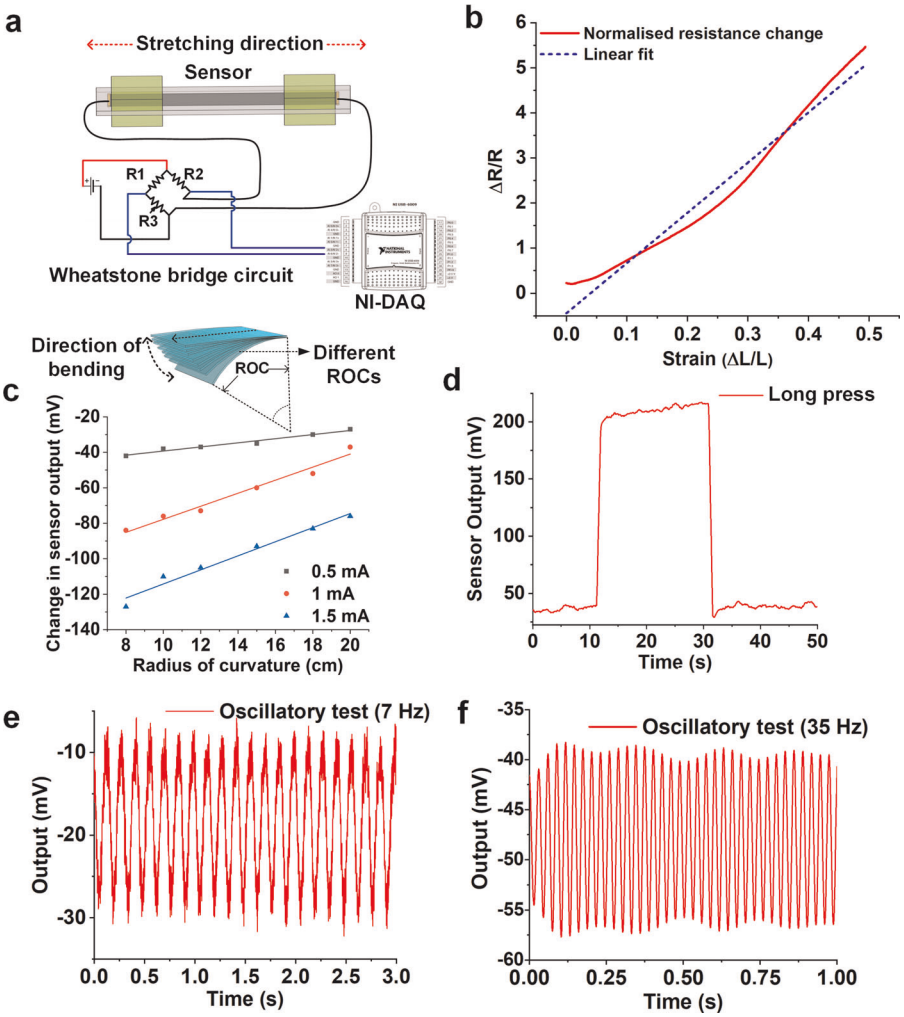

Fig. 7 Response plots of CNF bundle strain sensor. a Schematic representation of the experimental setup for the tensile strain sensing characterization. **b** Plot of averaged resistance change versus tensile strain in the CNF-PDMS strain sensor for tensile strains up to 50%. **c** Static bending test. **d** Long press test. **e** Response at 7 Hz dipole stimulus. **f** Response at 35 Hz dipole stimulus.

Table 2. Comparing the gauge factors of various flexible strain sensors reported in the literature.

Material	Gauge factor	Linearity
Carbon Black-PDMS[25]	1.8−5.5	Two linear regions
Carbon Black-Ecoflex[39]	3.8	Nonlinear
Single CNF strain sensor[35]	1.96−2.55	Linear
Graphene-Rubber[33]	35	Linear and exponential regions
Graphene ink-on-PDMS[40]	37	Linear
Graphene-PDMS foam[23]	2.87−8.77	Two linear regions
CNTs-Ecoflex[21]	1−2.5	Linear
CNF bundle (This work)	11.14	Linear

METHODS

Electrospinning of PAN nanofibers

Polyacrylonitrile powder (MW 150,000 g/mol) and *N*,*N*-dimethylformamide (DMF), purchased from Sigma-Aldrich, Netherlands, were used to form the PAN nanofiber bundles. PAN powder was dissolved in DMF solvent to obtain a 9% (w/v) solution. Stirring the solution at 30 °C for 120 min using a hot-plate magnetic stirrer homogeneously dissolved the PAN powder and formed a clear and viscous polymer solution. Electrospinning setup from Inovenso™ electrospinner fitted with a stainless-steel rotating mandrel collector was used for electrospinning PAN nanofibers. A rotating mandrel collector spinning at high speed allowed in situ alignment of the nanofibers. A standard syringe pump fixed with a 10 ml syringe was used to feed the PAN polymer solution through a needle (18G) at a constant flow rate of 1 ml/h. A constant temperature of 22 °C was recorded inside the electrospinning setup. The rotating spindle collector, 10 cm in diameter was covered with aluminum (Al) foil and set to rotate at a constant speed of 1500 rpm and a direct current (DC) voltage of 12 kV was applied between the collector and the conducting needle tip. A gap of 15 cm was maintained between the needle tip and base of the rotating mandrel collector. The electrospinning process was carried out for 30 min to obtain a film of uniform nanofibers deposited on an aluminum foil substrate. In addition, isolated single nanofibers were obtained on specially designed MEMS substrates for demonstrating the capability of using the piezo-resistive CNFs for flow sensing applications.

Pyrolyzation of the PAN precursor

The electrospun nanofiber bundles were initially transferred from the aluminum foil substrate to a ceramic crucible for high temperature pyrolyzation process. For stabilization and subsequent pyrolysis, the nanofiber mats were placed in a programmable ceramic tube furnace. For the first step involving stabilization to form a layer of oxide, the

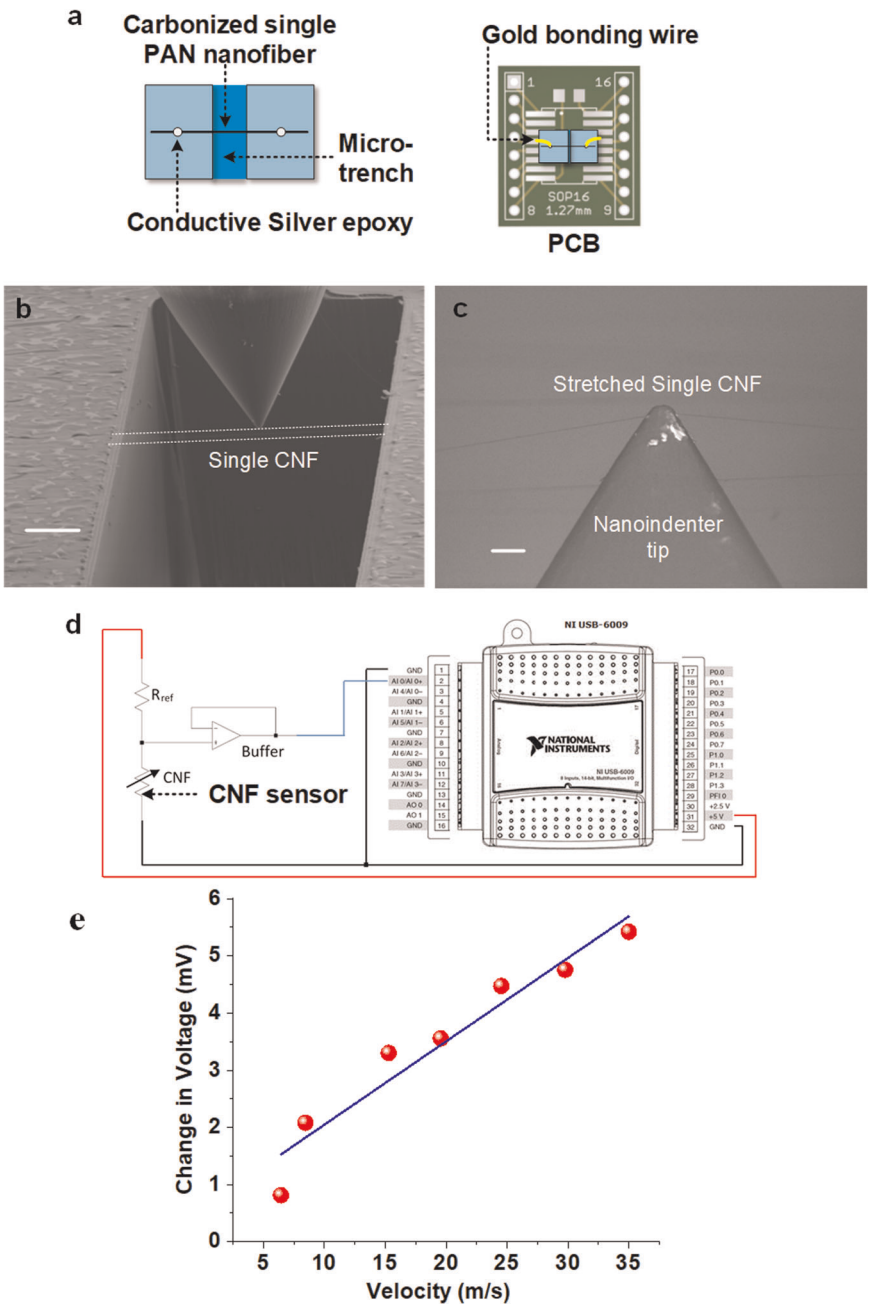

Fig. 8 Images and plots for flow sensing employing a single carbon nanofiber. a Schematic representation of the single CNF on the MEMS substrate bonded on to a printed circuit board for wind tunnel test. **b** SEM micrograph of the nanoindenter tip positioned over an isolated CNF secured on a microfabricated substrate. **c** SEM micrograph of the isolated CNF stretched by the nanoindenter tip to demonstrate its stretchability. **d** Circuit schematic representing the data acquisition setup for the single CNF air flow sensor. **e** Plot showing the change in voltage across a single CNF in response to increasing wind flow velocity. Scale bars (**b**) = 100 µm; (**c**) = 10 µm.

nanofibers were heat-treated at a temperature of 245 °C for 60 min in the presence of air. A constant ramp rate of 5 °C/min was used to ramp-up and ramp-down the stabilization temperature. Following the stabilization, in order to conduct pyrolyzation, the tube furnace was sealed air-tight with a constant nitrogen (N_2) gas purge for 30 min to drive-out the air inside. Thereafter, the nanofibers were annealed in N_2 ambience at five different temperatures (500, 600, 700, 800, and 950 °C) to understand the effect of pyrolyzation temperature on the electrical and morphological characteristics of the synthesized CNFs. The stabilized nanofibers are ramped at a constant rate of 5 °C/min to the target annealing temperature (500/600/700/800/950 °C) where they were held for an hour before ramping down to the room temperature at the same ramp rate. A flow chart illustrating the process steps from electrospinning to carbonization is provided in the Supplementary Information (Supplementary Fig. 1).

Morphology of the carbon nanofibers

The morphologies of the synthesized CNFs were studied using an FEI Nova NanoSEM 230 field-emission scanning electron microscope (FE-SEM). The reported diameters of the nanofibers carbonized at the different annealing temperatures were average values of several measurements.

Compositional analyses

The chemical and compositional changes in the electrospun PAN nanofibers after stabilization and annealing were studied by employing Raman and X-ray photoelectron spectroscopic analyses. Renishaw inVia Raman microscope (532 nm (green) diode laser with 1800 l/mm grating) was used for Raman spectroscopy. All the pyrolyzed nanofiber bundles were studied using the aforementioned Renishaw inVia Raman

microscope. For having a spot size of 0.5 µm, "High Confocal" mode was selected. One percent of the 34.1 mW laser source power was employed, and the scans were acquired in static acquisition mode and averaged over 100 accumulations. Raman analyses were performed on all the CNF samples pyrolyzed at various temperatures to study the effect of pyrolyzation temperature on the formation of D- and G-peaks. Thermo ESCALAB250Xi X-ray photoelectron spectrometer was used for performing XPS to study the change in the surface composition of the nanofibers over different annealing temperatures. FEI Nova NanoSEM 230 fitted with a Bruker SDD-EDS detector was used for performing EDX analyses on the samples to study the change in relative elemental composition with different pyrolyzation temperatures (results not shown). Transmission electron microscopy (TEM) imaging was conducted on the samples to study the formation of any lattice structures due to graphitization. The individual nanofiber samples were sputtered with ~25 nm of gold and the cross-section TEM lamella of an individual nanofiber was milled using an FEI xT Nova Nanolab 200 dual-beam workstation. The TEM lamella specimens were then placed on a standard carbon film Cu grid using an ex situ lift-out method. TEM data were obtained using a Philips CM200 field emission gun transmission electron microscope (FEG/TEM) equipped with a Bruker energy dispersive X-ray (EDAX) spectroscopy system operating at an accelerating voltage of 200 kV. Data obtained from the TEM experiment includes bright-field TEM images, energy dispersive spectroscopy (EDS) and selected area diffraction.

Electrical measurement

For measuring the effect of pyrolyzation temperature on the resistance, 10 × 10 mm CNF bundles were cut and sized. The thickness of each bundle was measured to be uniform (~10 µm). Cascade probe station was used to measure the overall variation of the resistance in the pyrolyzed nanofiber mats with increasing annealing temperature.

Circuits and sensor data acquisition

For demonstrating the capability of the sensor in detecting constant pressure and dynamic stimuli, a balanced Wheatstone bridge circuit was designed, to which the strain sensor was connected as one arm of the bridge circuit. The dynamic strain stimuli to the sensor was delivered by employing an 8 mm sphere connected to a Brüel & Kjær permanent magnet mini-shaker by a 120 mm long steel rod having a diameter of 2 mm. The sphere was driven at the desired frequencies using a function generator connected to a power amplifier (Brüel & Kjær model number 2718). The output of the balanced bridge was acquired through National instruments data acquisition system (DAQ, NI USB-6009) and recorded using National Instruments LabView software. For the case of static bending curvature measurement, appropriate potential divider circuits were designed, and a constant current source was used for supplying a constant bias current. For all the sensor tests mentioned above, the voltage outputs from sensors were acquired at a sampling rate of 2 kHz. For all the sensing experiments involving Wheatstone bridge circuits, a 9 V constant D.C. power supply was used for biasing the corresponding bridges. For all the experimental results, unamplified outputs of the sensor were plotted.

Flow sensing in wind tunnel

For demonstrating the capability of a single CNF for flow sensing applications, TECHQUIMENT AF1125, wind tunnel setup was used. The single CNF sensor was connected in series to a reference resistor (R_{ref}) and the voltage across the CNF was connected to the input of a voltage buffer. The output of the voltage buffer was connected to the analog input (AI 0) of the NI-DAQ. The voltage divider circuit was driven by a 5 V_{DC} output of the DAQ. The chosen value of R_{ref} was approximately 1.5 MΩ, which is approximately half of the CNF resistance. Seven arbitrary wind velocities from 0 to 35 m/s were tested and the changes in voltage across the single nanofiber were logged by the NI-DAQ, NI USB-6009, at 2 kHz sampling rate. Each velocity was performed for at least 60 s and the data captured by the NI-DAQ are processed with Origin Pro for data averaging. Further details of the wind tunnel test have been provided in the Supplementary Information (Supplementary Fig. 5).

DATA AVAILABILITY

The data that support the findings of this study are available from the corresponding author upon reasonable request.

Received: 23 October 2019; Accepted: 15 April 2020;
Published online: 20 May 2020

REFERENCES

1. Aktakka, E. E., Peterson, R. L. & Najafi, K. A CMOS-compatible piezoelectric vibration energy scavenger based on the integration of bulk PZT films on silicon. In *Technical Digest—International Electron Devices Meeting, IEDM* (IEEE, 2010).
2. Wang, X. Y., Lee, C. Y., Peng, C. J., Chen, P. Y. & Chang, P. Z. A micrometer scale and low temperature PZT thick film MEMS process utilizing an aerosol deposition method. *Sens. Actuators, A Phys.* **143**, 469–474 (2008).
3. Chen, X., Xu, S., Yao, N. & Shi, Y. 1.6 V nanogenerator for mechanical energy harvesting using PZT nanofibers. *Nano Lett.* **10**, 2133–2137 (2010).
4. Wang, Z. L. & Song, J. Piezoelectric nanogenerators based on zinc oxide nanowire arrays. *Science (80−.).* **312**, 242–246 (2006).
5. Qin, Y. et al. Microfibre-nanowire hybrid structure for energy scavenging. *Nature* **451**, 809–813 (2008).
6. Wang, X., Song, J., Liu, J. & Wang, Z. L. Direct-current nanogenerator driven by ultrasonic waves. *Science (80−.).* **316**, 102–105 (2007).
7. Sengupta, D. et al. Characterization of single polyvinylidene fluoride (PVDF) nanofiber for flow sensing applications. *AIP Adv.* **7**, 105205 (2017).
8. Liu, Z. H., Pan, C. T., Lin, L. W., Huang, J. C. & Ou, Z. Y. Direct-write PVDF nonwoven fiber fabric energy harvesters via the hollow cylindrical near-field electrospinning process. *Smart Mater. Struct.* **23**, 025003 (2014).
9. Sencadas, V., Moreira, M. V., Lanceros-Méndez, S., Pouzada, A. S. & Gregório Filho, R. α- to β transformation on PVDF films obtained by uniaxial stretch. *Mater. Sci. Forum* **514–516**, 872–876 (2006).
10. Dargaville, T. R. T. et al. Characterization, performance and optimization of PVDF as a piezoelectric film for advanced space mirror concepts. SAND2005-6846. p. 045009 (Sandia National Laboratories, 2005).
11. Wang, Y. R., Zheng, J. M., Ren, G. Y., Zhang, P. H. & Xu, C. A flexible piezoelectric force sensor based on PVDF fabrics. *Smart Mater. Struct.* **20** (2011).
12. Sengupta, D., Kottapalli, A. G. P., Miao, J. & Kwok, C. Y. Electrospun polyvinylidene fluoride nanofiber mats for self-powered sensors. In *2017 IEEE SENSORS* 1–3 (IEEE, 2017).
13. Asadnia, M. et al. From biological cilia to artificial flow sensors: biomimetic soft polymer nanosensors with high sensing performance. *Sci. Rep.* **6**, 32955 (2016).
14. Mandal, D., Yoon, S. & Kim, K. J. Origin of piezoelectricity in an electrospun poly (vinylidene fluoride-trifluoroethylene) nanofiber web-based nanogenerator and nano-pressure sensor. *Macromol. Rapid Commun.* **32**, 831–837 (2011).
15. Chang, J., Dommer, M., Chang, C. & Lin, L. Piezoelectric nanofibers for energy scavenging applications. *Nano Energy* **1**, 356–371 (2012).
16. Chang, C., Tran, V. H., Wang, J., Fuh, Y. K. & Lin, L. Direct-write piezoelectric polymeric nanogenerator with high energy conversion efficiency. *Nano Lett.* **10**, 726–731 (2010).
17. Bora, M., Kottapalli, A. G. P., Miao, J. & Triantafyllou, M. S. Biomimetic hydrogel-CNT network induced enhancement of fluid-structure interactions for ultra-sensitive nanosensors. *NPG Asia Mater.* **9**, e440 (2017).
18. Alamusi et al. Piezoresistive strain sensors made from carbon nanotubes based polymer nanocomposites. *Sensors* https://doi.org/10.3390/s111110691 (2011).
19. Pang, Y. et al. Flexible, highly sensitive, and wearable pressure and strain sensors with graphene porous network structure. *ACS Appl. Mater. Interfaces* https://doi.org/10.1021/acsami.6b08172 (2016).
20. Zhao, J. et al. Ultra-sensitive strain sensors based on piezoresistive nanographene films. *Appl. Phys. Lett.* https://doi.org/10.1063/1.4742331 (2012).
21. Amjadi, M., Yoon, Y. J. & Park, I. Ultra-stretchable and skin-mountable strain sensors using carbon nanotubes-Ecoflex nanocomposites. *Nanotechnology* https://doi.org/10.1088/0957-4484/26/37/375501 (2015).
22. Qin, Y. et al. Mechanically flexible graphene/polyimide nanocomposite foam for strain sensor application. https://doi.org/10.1021/acsnano.5b02781 (2015).
23. Sengupta, D., Pei, Y. & Kottapalli, A. G. P. Ultra-light weight and 3D squeezable graphene-polydimethylsiloxane composite foams as piezoresistive sensors. *ACS Appl. Mater. Interfaces* https://doi.org/10.1021/acsami.9b11776 (2019).
24. Yamada, T. et al. A stretchable carbon nanotube strain sensor for human-motion detection. *Nat. Nanotechnol.* https://doi.org/10.1038/nnano.2011.36 (2011).
25. Kong, J.-H., Jang, N.-S., Kim, S.-H. & Kim, J.-M. Simple and rapid micropatterning of conductive carbon composites and its application to elastic strain sensors. *Carbon* **77**, 199–207 (2014).
26. Amjadi, M. et al. Highly stretchable and sensitive strain sensor based on silver nanowire and elastomer nanocomposite. https://doi.org/10.1021/nn501204t (2014).

27. Sengupta, D. et al. Flexible Graphitized Polyacrylonitrile Nanofiber Bundles for Strain Sensors. In *NEMS 2018—13th Annual IEEE International Conference on Nano/Micro Engineered and Molecular Systems*, Singapore (2018).
28. Liu, H. et al. Lightweight conductive graphene/thermoplastic polyurethane foams with ultrahigh compressibility for piezoresistive sensing. *J. Mater. Chem. C* **5**, 73–83 (2017).
29. Zhang, S. et al. Ultrasensitive and highly compressible piezoresistive sensor based on polyurethane sponge coated with a cracked cellulose nanofibril/silver nanowire layer. *ACS Appl. Mater. Interfaces* **11**, 10922–10932 (2019).
30. Huang, T. et al. Porous fibers composed of polymer nanoball decorated graphene for wearable and highly sensitive strain sensors. *Adv. Funct. Mater.* https://doi.org/10.1002/adfm.201903732 (2019).
31. Liu, Q., Chen, J., Li, Y. & Shi, G. High-performance strain sensors with fish-scale-like graphene-sensing layers for full-range detection of human motions. *ACS Nano* https://doi.org/10.1021/acsnano.6b03813 (2016).
32. Yao, H. et al. Communication: A flexible and highly pressure-sensitive graphene—polyurethane sponge based on fractured microstructure design. *Adv. Mater.* https://doi.org/10.1002/adma.201303041 (2013).
33. Boland, C. S. et al. Sensitive, high-strain, high-rate bodily motion sensors based on graphene-rubber composites. *ACS Nano.* https://doi.org/10.1021/nn503454h (2014).
34. Zussman, E. et al. Mechanical and structural characterization of electrospun PAN-derived carbon nanofibers. *Carbon* **43**, 2175–2185 (2005).
35. Cai, J., Chawla, S. & Naraghi, M. Piezoresistive effect of individual electrospun carbon nanofibers for strain sensing. *Carbon* **77**, 738–746 (2014).
36. Kim, C. et al. Raman spectroscopic evaluation of polyacrylonitrile-based carbon nanofibers prepared by electrospinning. *J. Raman Spectrosc.* **35**, 928–933 (2004).
37. Knight, D. S. & White, W. B. Characterization of diamond films by Raman spectroscopy. *J. Mater. Res.* **4**, 385–393 (1989).
38. Matthews, M. J., Pimenta, M. A., Dresselhaus, G., Dresselhaus, M. S. & Endo, M. Origin of dispersive effects of the Raman D band in carbon materials. *Phys. Rev. B* **59**, R6585–R6588 (1999).
39. Muth, J. T. et al. Embedded 3D printing of strain sensors within highly stretchable elastomers. *Adv. Mater.* https://doi.org/10.1002/adma.201400334 (2014).
40. Kamat, A. M., Pei, Y. & Kottapalli, A. G. P. Bioinspired cilia sensors with graphene sensing elements fabricated using 3D printing and casting. *Nanomaterials* **9**, 954 (2019).

ACKNOWLEDGEMENTS

The authors acknowledge the financial support from ASTE Global Connection Bridging Fund for this project awarded to Dr. A. Michael. This research was also supported by the University of Groningen's start-up grant awarded to Dr. Ajay Kottapalli. We also thank the UNSW ANFF (NSW node) and UNSW MWAC for their support where much of the analytical work was done.

AUTHOR CONTRIBUTIONS

D.S. conducted the material and electrical characterization experiments and the associated data analysis. D.S. and S.-H.C. conducted the strain sensor fabrication, flow sensor fabrication, sensor testing and wrote the manuscript. S.L. prepared the nanofiber samples for FIB and carried out TEM imaging for nanofiber cross-section. A. G.P.K. conducted electrospinning, conceptualized the idea, and composed the experimental plan. A.M., C.Y.K. and A.G.P.K. conceived and supervised the project. Y.P. provided his insights into the material characterization. All authors contributed to the discussion of the results and to the critical reading of the manuscript.

COMPETING INTERESTS

The authors declare no competing interests.

ADDITIONAL INFORMATION

Supplementary information is available for this paper at https://doi.org/10.1038/s41528-020-0072-2.

Correspondence and requests for materials should be addressed to A.G.P.K.

Reprints and permission information is available at http://www.nature.com/reprints

Publisher's note Springer Nature remains neutral with regard to jurisdictional claims in published maps and institutional affiliations.